Center vortex geometry at finite temperature

Jackson A. Mickley , Waseem Kamleh , and Derek B. Leinweber
Centre for the Subatomic Structure of Matter, Department of Physics, The University of Adelaide,
South Australia 5005, Australia

The geometry of center vortices is studied in SU(3) gauge theory at finite temperature to capture the key structural changes that occur through the deconfinement phase transition. Visualizations of the vortex structure in temporal and spatial slices of the lattice reveal a preference for the vortex sheet to align with the temporal dimension above the critical temperature. This is quantified through a correlation measure. A collection of vortex statistics, including vortex and branching point densities, and vortex path lengths between branching points, are analyzed to highlight internal shifts in vortex behavior arising from the loss of confinement. We find the zero-temperature inclination of branching points to cluster at short distances vanishes at high temperatures, embodying a rearrangement of branching points within the vortex structure. These findings establish the many aspects of center vortex geometry that characterize the phase transition in pure gauge theory.

I. INTRODUCTION

The center vortex picture [1–4] is well established as a prime candidate for underpinning many of the emergent phenomena in quantum chromodynamics (QCD), including dynamical chiral symmetry breaking [5–11] and confinement [5,9,12–28]. Center vortices naturally give rise to an area-law falloff for large Wilson loops [29,30],

$$\langle W(C) \rangle \sim \exp\left(-\sigma A(C)\right), \tag{1}$$

with such behavior signifying confinement for static heavy quarks [4,31–33]. Due to string breaking at large separations [34], in the presence of light quarks one can turn to the gluon propagator, where, if there is no Källen-Lehmann representation, the corresponding physical states are confined. This is often inferred by studying the Schwinger function of the gluon propagator, for which negative values at large Euclidean times signal positivity violation in the spectral density function [35,36].

In SU(2) Yang-Mills theory, center vortices have been demonstrated to account for 100% of the string tension σ [12,15], though full recovery in pure SU(3) theory has proven more challenging. Despite vortex removal resulting in a vanishing string tension, static quark potential calculations on vortex-only fields has shown to recover only $\approx$

62% of the string tension in SU(3) [25]. Remarkably, recent work considering the impact of dynamical fermions on center vortices for the first time showed that the string tension can be entirely recreated from center vortices in full QCD [27]. In addition, the vortex-removed fields display no signs of positivity violation with dynamical fermions, another advantage compared to the pure gauge theory which still exhibited a remnant effect at long distances [28]. These findings reaffirm center vortices as fundamental to the nonperturbative nature of confinement, though the inconsistencies in the pure gauge regime remain an open problem.

Following a phase transition at some critical temperature T_c, the SU(N) vacuum is understood to exist in a deconfined state. This motivates exploring center vortices at a range of temperatures through the deconfinement phase transition in SU(3) to identify the principal structural changes that can be attributed to confinement. We utilize previously developed visualization techniques [37] to qualitatively study the changes in vortex geometry. This is followed by a focused analysis into several vortex statistics as a function of temperature, such as vortex and branching point densities. Given they do not occur in SU(2), branching points provide a particularly interesting avenue of research, and vortex branching is known to experience substantial bulk changes at T_c [26,38]. We subsequently take this further by studying the distances between successive branching points and the accompanying branching probabilities, in turn searching for any internal rearrangement of branching points at high temperatures. In this regard, the pure gauge theory provides fertile ground for drawing out the salient features of vortex

geometry at finite temperature that can guide future work with the inclusion of dynamical fermions in QCD.

This paper is structured as follows. In Sec. II, the center vortex model is briefly reviewed along with the procedure for identifying vortices on the lattice. Section III contains visualizations of the vortex structure at a range of temperatures either side of T_c and the accompanying discussion. Our detailed analysis on the evolution of intrinsic vortex statistics with temperature is presented throughout Secs. IV and V. Finally, we summarize our main findings in Sec. VI. Supplemental Material providing embedded animations of center vortex structures is located at Ref. [39]. Instructions on interacting with these animations is given therein, and the figures are referenced in the main text as Fig. S-x.

II. CENTER VORTICES

Center vortices, originally introduced in Ref. [1], are regions of the gauge field that carry magnetic flux quantized according to the center of SU(3),

$$\mathbb{Z}_3 = \left\{ \exp\left(\frac{2\pi i}{3} n\right) \mathbb{I} \;\middle|\; n = -1, 0, 1 \right\}. \qquad (2)$$

Physical vortices in the QCD ground-state fields have a finite thickness and so permeate all four spacetime dimensions. In contrast, on the lattice "thin" center vortices are extracted through a well-known gauge-fixing procedure that seeks to bring each link variable $U_\mu(x)$ as close as possible to an element of $\mathbb{Z}_3$, known as maximal center gauge. These thin vortices form closed surfaces in four-dimensional Euclidean spacetime, and thus one-dimensional structures in a three-dimensional slice of the four-dimensional spacetime.

Fixing to maximal center gauge is typically performed by finding the gauge transformation $\Omega(x)$ to maximize the functional [40]

$$R = \frac{1}{V N_{\text{dim}} N_c^2} \sum_{x,\mu} |\text{Tr} U_\mu^\Omega(x)|^2, \qquad V = N_s^3 \times N_t. \qquad (3)$$

The links are subsequently projected onto the center,

$$U_\mu(x) \longrightarrow Z_\mu(x) = \exp\left(\frac{2\pi i}{3} n_\mu(x)\right) \mathbb{I} \in \mathbb{Z}_3, \qquad (4)$$

with $n_\mu(x) \in \{-1, 0, 1\}$ identified as the center phase nearest to $\arg \text{Tr} U_\mu(x)$ for each link. Finally, the locations of vortices are identified by nontrivial plaquettes in the center-projected field,

$$P_{\mu\nu}(x) = \prod_\square Z_\mu(x) = \exp\left(\frac{2\pi i}{3} m\right) \mathbb{I} \qquad (5)$$

with $m = \pm 1$. The value of m is referred to as the *center charge* of the vortex, and we say the plaquette is pierced by a vortex.

Due to a Bianchi identity satisfied by the projected vortex fields [26,38], the center charge is conserved such that the vortex topology manifests as closed sheets in four dimensions, or as closed lines in three-dimensional slices of the lattice. Although gauge-dependent, numerical evidence strongly suggests the projected vortices' locations are correlated with the physical "thick" vortices of the original fields [15,22,25,40,41]. This allows one to investigate the significance of center vortices through the projected links $Z_\mu(x)$.

The connection between center vortices and confinement is apparent through space-time Wilson loops of size $R \times T$, which asymptotically give access to the static quark-antiquark potential $V(r)$,

$$\langle W(R,T) \rangle \sim \exp(-V(r) aT), \qquad r = Ra, \quad T \text{ large.} \qquad (6)$$

The percolation of center vortices through spacetime implies an area law for the Wilson loop, Eq. (1) [19–21,29], which allows one to extract a potential $V(r)$ that linearly rises with the separation r. In the confined phase, this has been seen in numerical simulations for both SU(2) [12,15] and SU(3) [22,25].

In contrast, center vortices in the deconfined phase amount to a vanishing quark-antiquark potential [18], signaled by a trivial expectation value for space-time Wilson loops. This is a natural consequence of vortices no longer percolating all four dimensions, indicating an inherent change to the bulk vortex structure as the critical temperature T_c is crossed. This alludes to the phase transition being geometric in nature, as also realized by a construction of center-*electric* fluxes [42]. In SU(2), it is understood the vortex sheet shifts to principally align with the temporal dimension, though the structure still percolates in the spatial dimensions [18–21]. This results specifically in an absence of vortices piercing space-time Wilson loops, and a trivial expectation value in Eq. (6) follows. The same overarching change is expected in SU(3), and initial numerical results support this conclusion [26,38]. We will elucidate this property by visualizing the center vortex structure below and above T_c and quantifying the observations with new statistical measures, thereby affirming the geometric nature of the deconfinement phase transition in QCD.

In this work, we utilize five pure-gauge ensembles of 100 configurations, two below T_c and three above T_c, each with a spatial volume of 32^3 and fixed isotropic lattice spacing $a = 0.1$ fm. The ensembles are generated using Hybrid Monte Carlo [43,44] with an Iwasaki renormalization-group improved action [45,46]. The temporal extents and corresponding temperatures are summarized in Table I, where we take $T_c = 270$ MeV [47].

TABLE I. The number of sites N_t in the temporal dimension and corresponding temperatures, both in MeV and in terms of the critical temperature $T_c = 270$ MeV, for each ensemble.

N_t	T (MeV)	T/T_c
12	164.4	0.609
8	246.6	0.913
6	328.8	1.218
5	394.6	1.461
4	493.3	1.827

III. VISUALIZATIONS

We now move to qualitatively analyze the center vortex structure at finite temperature, drawing on visualization techniques previously established in Ref. [37]. The basic construction is reiterated briefly here. Vortices exist on the dual lattice. This allows the plaquette in the center-projected field to be written as [26,38]

$$P_{\mu\nu}(x) = \exp\left(\frac{\pi i}{3}\epsilon_{\mu\nu\kappa\lambda}m_{\kappa\lambda}(\bar{x})\right), \qquad (7)$$

where $\bar{x} = x + \frac{a}{2}(\hat{\mu} + \hat{\nu} - \hat{\kappa} - \hat{\lambda})$ and $m_{\kappa\lambda}(\bar{x}) \in \{-1, 0, 1\}$ defines the oriented center charge of the plaquette, such that $m_{\kappa\lambda}(\bar{x}) = -m_{\lambda\kappa}(\bar{x})$.

To construct a 3D visualization we slice over a given dimension, which corresponds to fixing the value of λ in Eq. (7). This leaves one orthogonal direction $\hat{\kappa}$ in the three-dimensional slice that can be used to identify the plaquette. For each nontrivial plaquette, the vortex is accordingly rendered as a jet pointing in the $m_{\kappa\lambda}(\bar{x})\hat{\kappa}$ direction and piercing the plaquette. Due to the presence of the Levi-Civita symbol in Eq. (7), this effectively corresponds to implementing a right-hand rule for the orientation of the jet. As such, the visualizations exclusively show the flow of $m = +1$ center charge. This convention is demonstrated in Fig. 1.

Utilizing the SU(3) cluster identification algorithm developed in Ref. [48], we present typical vortex structures
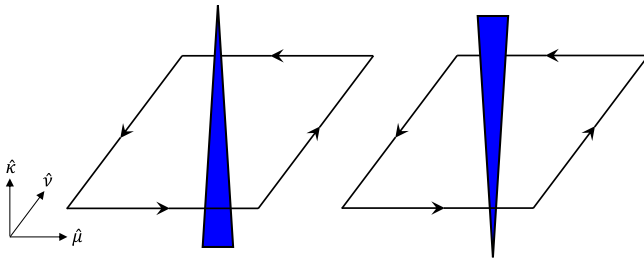

FIG. 1. The visualization convention for center vortices. An $m = +1$ vortex (left) is represented by a jet in the available orthogonal dimension, with the direction given by the right-hand rule. An $m = -1$ vortex (right) is rendered by a jet in the opposite direction.

in three-dimensional slices at increasing temperature in Figs. 2–6. We separately show the structure in temporal slices ($\lambda = 4$) and spatial slices ($\lambda = 1, 2, 3$), which is important to reveal the primary features of the phase transition. The structure in the spatial slices is insensitive to the choice of spatial dimension sliced over, and thus we present visualizations for the x dimension ($\lambda = 1$).

In the confined phase (Figs. 2 and 3), the visualizations reveal a single large percolating cluster (colored in blue) that dominates the vortex structure in both temporal and spatial slices. A handful of smaller secondary clusters are scattered throughout the lattice. This is consistent with previous observations on near-zero temperature pure gauge configurations [37,48], indicating the external features of the vortex structure remain unchanged as we approach the critical temperature from below.

Moving above the critical temperature (Figs. 4–6) results in a shift in the behavior of vortex matter. Clearly, the temporal and spatial structures diverge. The temporal slices are still dominated by a single large connected cluster, indicating the vortex structure remains percolating in the spatial dimensions. In contrast, the spatial slices instead reveal an abundance of small vortex clusters mostly parallel to the short temporal dimension, which are closed under periodic boundary conditions. This establishes that the vortex sheet in the deconfined phase principally aligns with the temporal dimension, matching the observation in SU(2). As a timelike surface, the vortex sheet rarely cuts through space-time plaquettes above T_c. This underlies the strong preference for vortices to pierce space-space plaquettes in spatial slices, which are oriented with the temporal axis.

Nonetheless, not all clusters wind around the temporal dimension, and there are still remnant fluctuations where a vortex line "twists" to temporarily propagate in a spatial dimension. This latter effect could be in part due to ambiguity in the precise location of projected vortices within the physical "thick" center vortices [15]. Still, the most significant feature of the spatial slices above the critical temperature is an absence of vortex lines that span the spatial extent and pierce opposite space-time faces, demonstrating a collapse in vortex geometry that results in the loss of percolation.

To elaborate on this, we provide animations over the temporal and spatial slices for each temperature throughout Figs. S-1–S-5 in the Supplemental Material [39]. This aids in understanding the four-dimensional nature of the center vortex sheet. Below T_c, the vortex structure changes considerably on a per-slice basis in both temporal and spatial slices, with the vortex lines moving erratically around the lattice. This simply indicates the vortex sheet is not aligned with any particular dimension, implying the observed three-dimensional structure depends on where one slices. The animations above T_c are more intriguing. In temporal slices, the vortex structure is effectively "frozen," only experiencing a slight shimmer or oscillation from slice
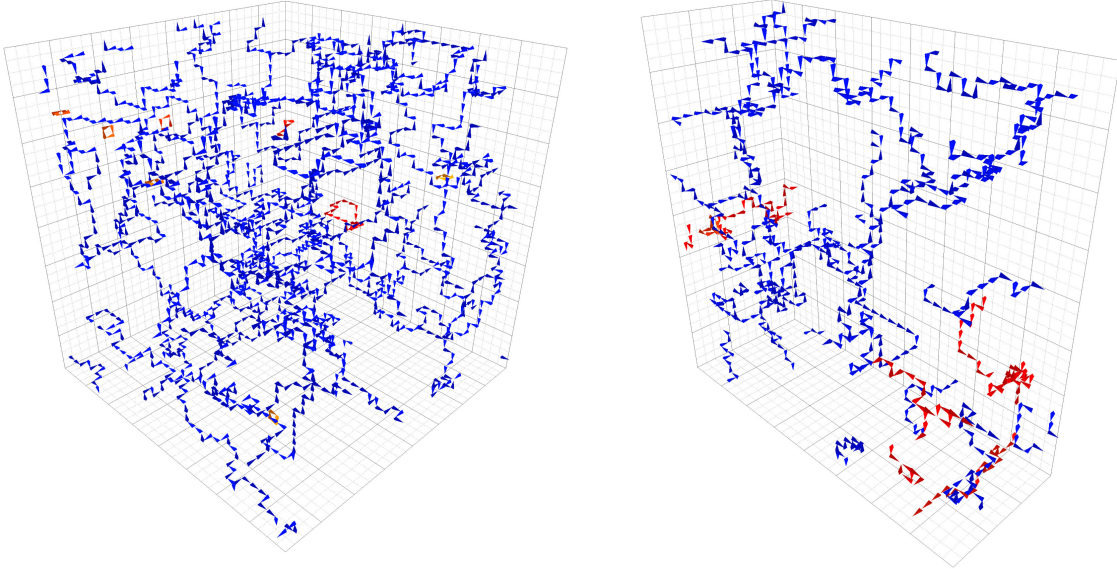
FIG. 2. Center vortex structure in temporal slices (left) and spatial slices (right) below the critical temperature at $T = 0.609T_c$. In this and the following four illustrations, the shorter dimension in the right-hand visualization is the temporal direction.
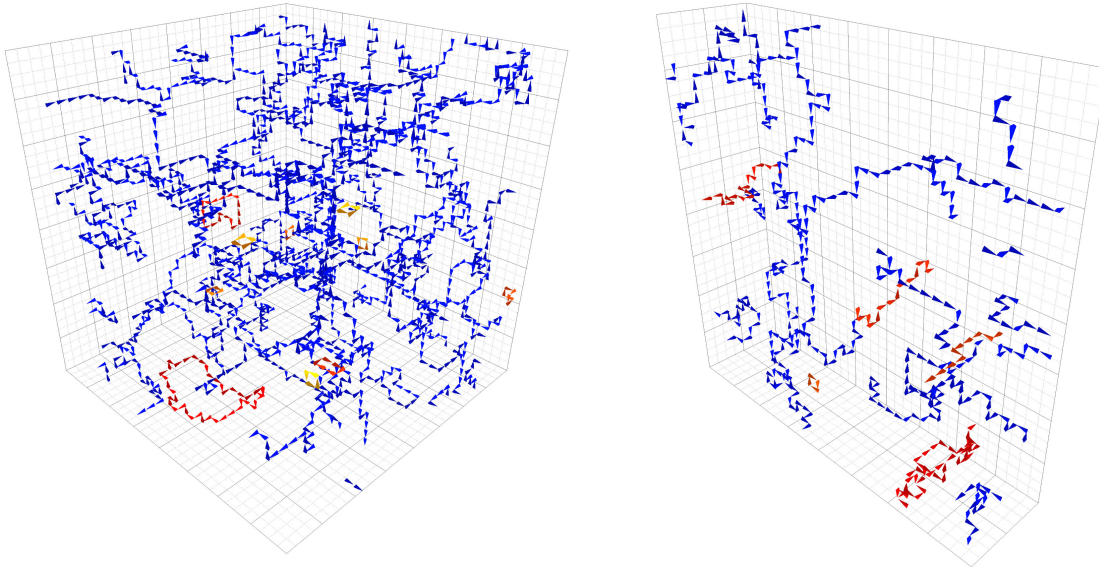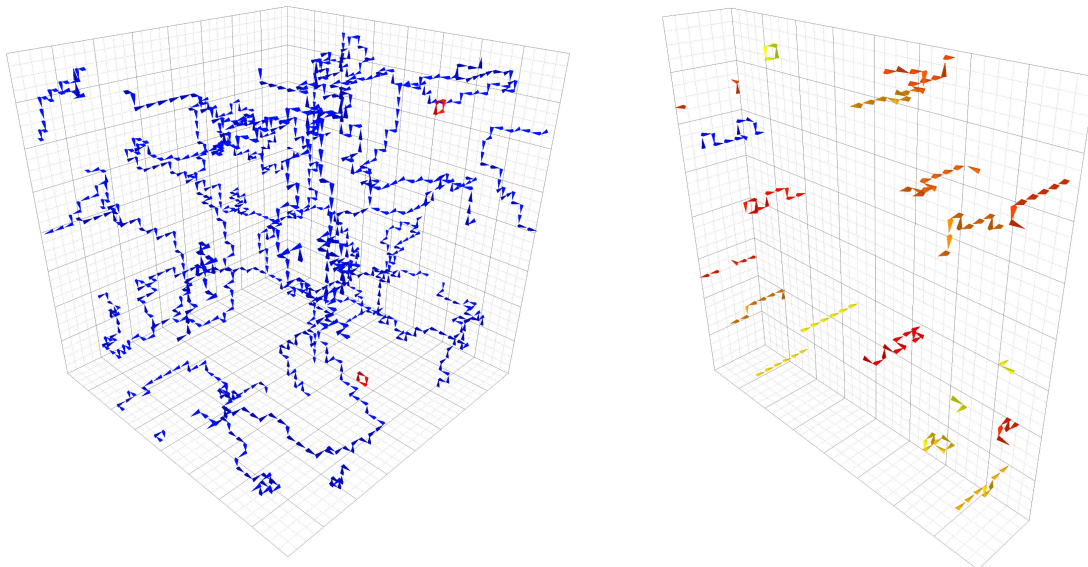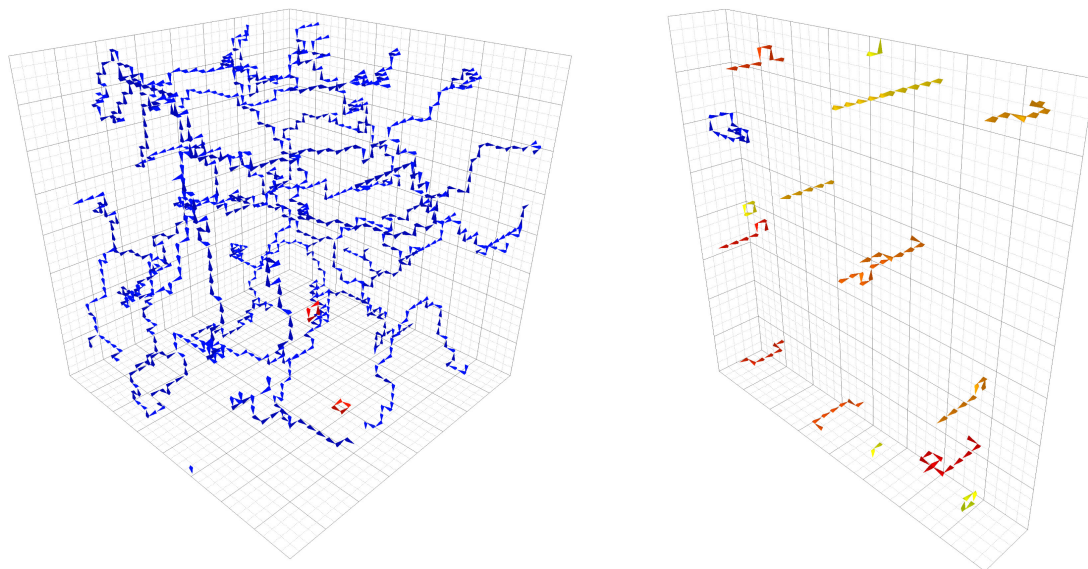

FIG. 3. Center vortex structure in temporal slices (left) and spatial slices (right) below the critical temperature at $T = 0.913T_c$.

to slice. This is yet another manifestation that the vortex sheet is oriented with the temporal dimension, as this signifies the spatial structure is predominantly unchanged regardless of where along the Euclidean time dimension one slices. On the other hand, animating over the spatial slices above T_c shows there is still substantial change in the position of the short vortex lines. This is a consequence of the fact that the center vortex sheet still percolates in the spatial dimensions.

For an analogy to the deconfined phase, one can imagine a three-dimensional cylinder aligned with the z axis. If slicing along said z dimension, one would find an identical circle regardless of where the slice is taken, which is the equivalent scenario to slicing the center vortex structure through the temporal dimension. By contrast, slicing along the x or y dimensions would result in two disconnected lines parallel to the z axis. Importantly, the position of and distance between these lines varies depending on the slice coordinate. This matches the arrangement of vortices in spatial slices, with many disconnected clusters winding around the temporal dimension but still moving over the lattice through each slice.

At this point, an essential consideration is whether the alignment of the vortex sheet is a genuine dynamical effect,

FIG. 4.   Center vortex structure in temporal slices (left) and spatial slices (right) above the critical temperature at $T = 1.218T_c$.

FIG. 5.   Center vortex structure in temporal slices (left) and spatial slices (right) above the critical temperature at $T = 1.461T_c$.

or a byproduct of algorithmic issues. For instance, it could indicate the presence of nonergodicity in the Markov chain of lattice QCD, with the persistent alignment observed throughout the ensemble due to topological locking. Another possibility is that the alignment arises specifically from the low number of temporal lattice sites required at high temperatures on coarser lattices. These concerns are especially prescient with the context that vortices are stiff [21,26], such that configurations in the deconfined phase wherein the vortex sheet is not primarily aligned with the short temporal dimension are suppressed. We investigate these possibilities with greater detail in Sec. IV B. Using a novel measure to quantify the alignment through the

freezing of the vortex structure in temporal slices, we conclude the vortex sheet alignment with the temporal dimension is a genuine dynamical effect.

The fact temporal slices comprise a percolating cluster in both phases raises the question of whether any more subtle underlying changes occur to the vortex structure. Comparing Figs. 2–6, it is visually clear the primary cluster in the temporal slices experiences a significant reduction in density of vortex matter as the critical temperature is crossed. Subsequently, this low density appears to gradually increase as the temperature climbs away from T_c, with the cluster at our highest temperature nearly matching that found in the confined phase. There is also a plausible drop
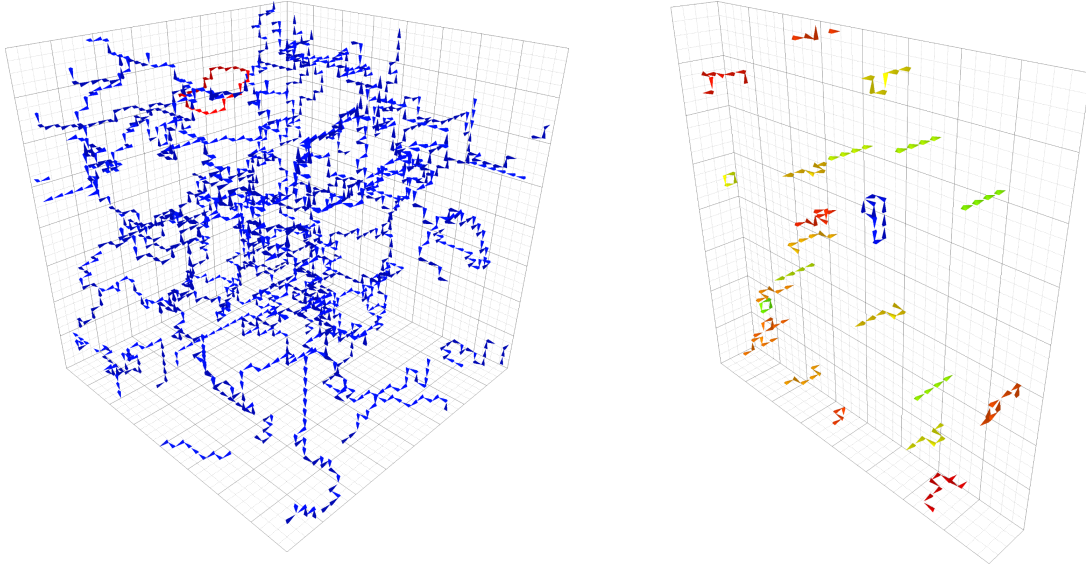
FIG. 6.   Center vortex structure in temporal slices (left) and spatial slices (right) above the critical temperature at $T = 1.827T_c$.

in the number of secondary clusters found in the temporal slices above T_c, though it is unclear whether this is representative of the entire ensemble or a consequence of the specific slices displayed. These statistics, along with several others, will be investigated quantitatively in the following section.

IV. VORTEX STATISTICS

Next, we investigate a number of statistical quantities related to center vortices to bring to light any additional structural changes not immediately apparent through visualization. Several such properties, such as vortex and branching point densities, have previously been investigated across the phase transition in SU(3) in Ref. [38], though here we extend this to a broader range of temperatures. We further analyze the secondary clusters present throughout the volume and compute a correlation of the vortex structure between various slices of the lattice. We defer our branching point analysis to Sec. V where we perform a thorough investigation into the geometry of branching points as a function of temperature.

In this section, we display an extra point at $T/T_c = 0.114$ on our plots using data from Ref. [48], obtained from a $32^3 \times 64$ ensemble of 200 configurations, but with otherwise identical properties to our finite-temperature ensembles. Statistical errors are calculated through the standard deviation of 100 bootstrap ensembles.

A. Vortex structure correlation

The key feature of the phase transition relevant to center vortices is the alignment of the vortex sheet with the temporal dimension. This manifests in time slices of the lattice as a vortex cluster that undergoes minimal changes between successive slices. For this reason, we seek to

calculate a correlation of the vortex structure between temporal slices as a means to quantify this change and investigate the extent to which it continues to evolve above T_c.

This is achieved by first defining the indicator function,

$$\chi_{ij}(\mathbf{x}, t; \tau) = \begin{cases} 1, & m_{ij}(\mathbf{x}, t)m_{ij}(\mathbf{x}, t + \tau) > 0 \\ 0, & \text{otherwise} \end{cases}, \quad (8)$$

which takes the value 1 if a nontrivial plaquette at spatial position $\mathbf{x}$ in time slice t is also pierced by a vortex in some later time slice $t + \tau$ with the same center charge. As we are looking in temporal slices, here $i, j = 1, 2, 3$. We can then define the correlation measure,

$$C(\tau) = \frac{1}{N_{\text{vor}} N_t} \sum_{\substack{\mathbf{x},t, \\ i,j}} \chi_{ij}(\mathbf{x}, t; \tau), \quad (9)$$

where N_{vor} is the average number of vortices per temporal slice. This normalization factor enforces the maximum value of $C(\tau)$ to 1, corresponding to the case the vortex structure is completely unchanging along the temporal dimension. Due to periodic boundary conditions, τ is restricted to $\tau \leq \lfloor N_t/2 \rfloor$. Consequently, we compare $\tau = 1, 2$ across all our ensembles. This evolution is presented in Fig. 7.

Below T_c, the correlation is found to be constant with $C(1)$ slightly above 0.2, whilst $C(2)$ unsurprisingly attains a substantially smaller value. It is natural to inquire as to whether one can infer any significance to these values. To do so, consider a slowly varying field such that a vortex sheet passes through two consecutive (three-dimensional) time slices with spatial positions in the neighborhood of each other. Then, it is reasonable to assume that a pierced
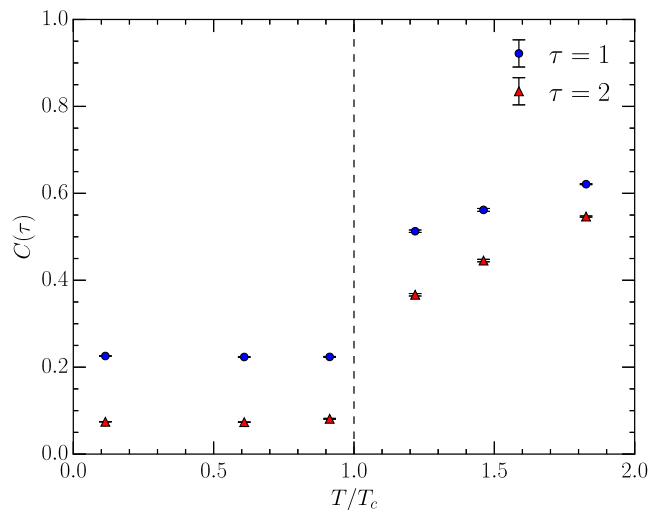
FIG. 7. The correlation $C(\tau)$ defined in Eq. (9) for $\tau = 1, 2$ as a function of temperature. It is constant below T_c, though it experiences a sudden jump at the phase transition where the vortices shift to principally align with the temporal dimension. Subsequently, it continues to increase above T_c.
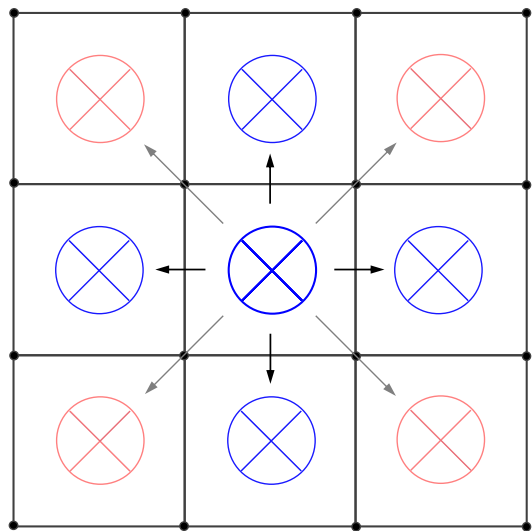

FIG. 8. An illustration of the mechanism underlying vortex correlations. Initially, the center plaquette is pierced by a vortex on some time slice. Provided there is some "smoothness" to the vortex structure, on the subsequent time slice it can either remain invariant or move to one of the surrounding plaquettes. In the simplest case, the vortex remains invariant or moves to one of the four directly adjacent plaquettes (dark arrows), corresponding to a probability of 1/5 that the center plaquette remains pierced on consecutive time slices. However, depending on the angle at which the vortex sheet passes through the time slice, the jet can also move to one of the four "diagonal" plaquettes (gray arrows). This implies a probability for the vortex to remain invariant of less than 1/5.

plaquette could either remain invariant or move to an adjacent plaquette. In the case that an equal probability is applied to each, there is a 1/5 chance that a vortex line piercing a given space-space plaquette proceeds to pierce the same plaquette one time step later, thus producing a contribution to Eq. (9). More generally, it is possible for the vortex sheet to pass through the three-dimensional slice at a sufficiently sharp angle that results in a jet on one slice moving a distance greater than the adjacent plaquette [37]. For example, it could additionally move to one of the neighboring diagonal plaquettes. Accounting for this possibility entails a probability smaller than 1/5 for the vortex to remain invariant. This idea is illustrated in Fig. 8.

However, we nonetheless find $C(1) > 1/5$, which can be attributed to a degree of "smoothness" arising from the physical interpretation of the system. As the lattice spacing a is decreased, $C(\tau)$ should increase (for fixed τ) in accordance with the smaller physical distance between consecutive temporal slices. It is therefore fascinating our value of $C(1)$ lies slightly above 1/5, indicating that a pierced plaquette typically tends to remain invariant or pierce one of the four adjacent plaquettes in consecutive slices. This physical smoothness in the vortex sheet can be seen in the supplementary animations (Figs. S-1–S-5) [39], where the movement of the vortex lines can to an extent be "tracked" between successive slices.

As the phase transition is crossed, Fig. 7 shows $C(\tau)$ undergo a jump as the vortex structure predominantly aligns with the temporal dimension. The correlation continues to grow as the temperature increases above T_c, signaling the alignment becomes stronger at higher T. It is as yet unclear whether $C(\tau)$ would eventually reach a value of 1 or instead plateau at some value < 1. Exploring the extent of the

alignment at even higher temperatures $T > 2T_c$ could be the subject of future work. Furthermore, the separation between $C(1)$ and $C(2)$ lessens as the temperature rises. This is expected since $C(\tau)$ necessarily becomes constant with τ (and equal to 1) if the vortex structure were completely frozen in the temporal dimension.

B. Investigation of algorithmic issues

Before proceeding, as promised we will utilize the correlation measure as a means to investigate the possibility that the vortex sheet alignment is attributed to an algorithmic effect. For this we consider two avenues. First, to test the ergodicity of the Markov chain we thermalize 100 independent hot starts on two $T > T_c$ ensembles with $N_t = 6$ and $N_t = 4$. If the alignment remains a consistent feature throughout these ensembles, then we can be assured it is not a result of any nonergodicity given each configuration started from an independent, completely random gauge field.

To explore a possible dependence on the gauge action, we perform this analysis using the standard Wilson action [31]. Therefore, to proffer a fair comparison we generate an additional zero-temperature ensemble on the account that different actions may produce slight differences in the precise quantitative behavior of vortex matter. The details

TABLE II. The β value, lattice spacing a, spatial and temporal extents N_s, N_t and the corresponding temperature for each ensemble used to investigate the alignment of the vortex sheet. The ensemble average of the correlation on consecutive slices $C(\tau = 1)$ is also given. Simulations are performed with the Wilson action. The scale is set using Sommer scale data from Ref. [49], where we take $r_0 \simeq 0.5$ fm.

β	a (fm)	N_s	N_t	T/T_c	$C(\tau = 1)$
5.96	0.10	32	64	0.114	0.1954(2)
			6	1.218	0.4027(11)
			4	1.827	0.4989(16)
6.42	0.05	64	12	1.218	0.4675(9)
			8	1.827	0.5182(4)

for these new ensembles are provided in Table II, along with the value of the correlation $C(\tau = 1)$ on each. We note that the value on the low-temperature ensemble of $C(1) \approx 0.195$ is slightly less than that from Fig. 7, indicating that the vortex matter recovered from the Wilson action tends to be "rougher" compared to the Iwasaki action of Refs. [45,46]. For this reason, we are content to accept smaller values of $C(1)$ at high temperature when compared against Fig. 7, though there should still be a consistent significant increase from zero temperature across the ensemble.

For $N_t = 6$ the correlation (in the ensemble average) has jumped from $C(1) \approx 0.195$ to $C(1) \approx 0.403$. The smallest value on any one configuration is ≈ 0.370, indicating the strong alignment is present in each thermalized hot start. This is also represented by the small statistical uncertainty seen in Table II. The same pattern is seen with $N_t = 4$, on which the ensemble average has climbed to $C(1) \approx 0.499$. In this ensemble, there is one particularly interesting case. A single $N_t = 4$ configuration exhibited a correlation value of $C(1) \approx 0.373$, a clear outlier compared to the next-smallest value of $C(1) \approx 0.479$. Although still displaying a preferential alignment with the temporal dimension compared to zero temperature, this configuration also featured two disconnected vortex lines winding around the long spatial dimensions. These inevitably pierce many additional space-time plaquettes. Such a configuration would likely not be obtained within a continuous Markov chain, highlighting the importance of thermalizing independent hot starts. That said, this was the only configuration from the set with such behavior. From this we conclude that the alignment of the vortex sheet as represented by the freezing in temporal slices is a genuine dynamical effect. It is not the upshot of nonergodicity in the Markov chain in the original set of ensembles.

The second avenue explored in this regard is the scaling of the alignment in taking the continuum limit at fixed temperature,

$$a \to 0, \qquad N_t \to \infty, \qquad T = (aN_t)^{-1} \text{ fixed.} \qquad (10)$$

For this purpose we generate two ensembles, again comprising 100 configurations, with half the lattice spacing as previously (i.e., $a = 0.05$ fm) but twice the lattice extent in all four dimensions. These accordingly have $N_t = 12$ and $N_t = 8$ for a direct comparison. The full details are also provided in Table II. By increasing the number of lattice sites in the temporal dimension, there are more chances for the vortex sheet to curve. We are concerned this could result in a softening of the alignment in the continuum limit, and hence it is critical to establish that the alignment persists to a similar degree after substantially diminishing the lattice spacing.

In fact, Table II reveals that the correlation has only increased in reducing a, in line with the discussion in the previous section regarding the physical "smoothness" of the vortex sheet. One might still be sceptical that the increase in value of $C(1)$ is mild compared to the factor of $1/2$ reduction in lattice spacing. However, it is important to bear in mind that since the lattice spacing has been decreased isotropically, the distance a jet must move to pierce an adjacent space-space plaquette, in relation to Fig. 8, is also physically smaller. These are competing effects which appear to approximately cancel each other out, resulting in the observed small increase in correlation between consecutive temporal slices. We therefore believe this indicates the overall extent of the alignment is approximately the same across our coarse and fine ensembles examined herein. If one were to instead utilize an anisotropic lattice, where exclusively the temporal spacing is decreased, we would expect this to effect a more substantial increase in the value of $C(\tau = 1)$.

We believe that this finding, in conjunction with the 100 independent hot starts, establishes the alignment and accompanying freezing in temporal slices as a physical effect rather than an algorithmic artefact. As a reference, in Fig. 9 we provide visualizations of a typical spatial slice from each of the four additional high-temperature ensembles analyzed in this section. Recall that the alignment manifests clearly in spatial slices as comprising primarily vortex lines which wind around the temporal axis. This is still seen to be true in each case here.

C. Vortex density

We now move to focus on the vortex area density, defined as the proportion of plaquettes pierced by a vortex. For a given three-dimensional lattice slice, this can be represented as

$$\hat{\rho}_{\text{vortex}} = \frac{\text{Number of nontrivial plaquettes in slice}}{3V_{\text{slice}}}, \qquad (11)$$

where V_{slice} is the number of lattice sites in the slice, and $\binom{3}{2} = 3$ counts the number of plaquettes at each site. We can then average over all slices along a given dimension. As defined in Eq. (11), $\hat{\rho}_{\text{vortex}}$ is a dimensionless quantity,
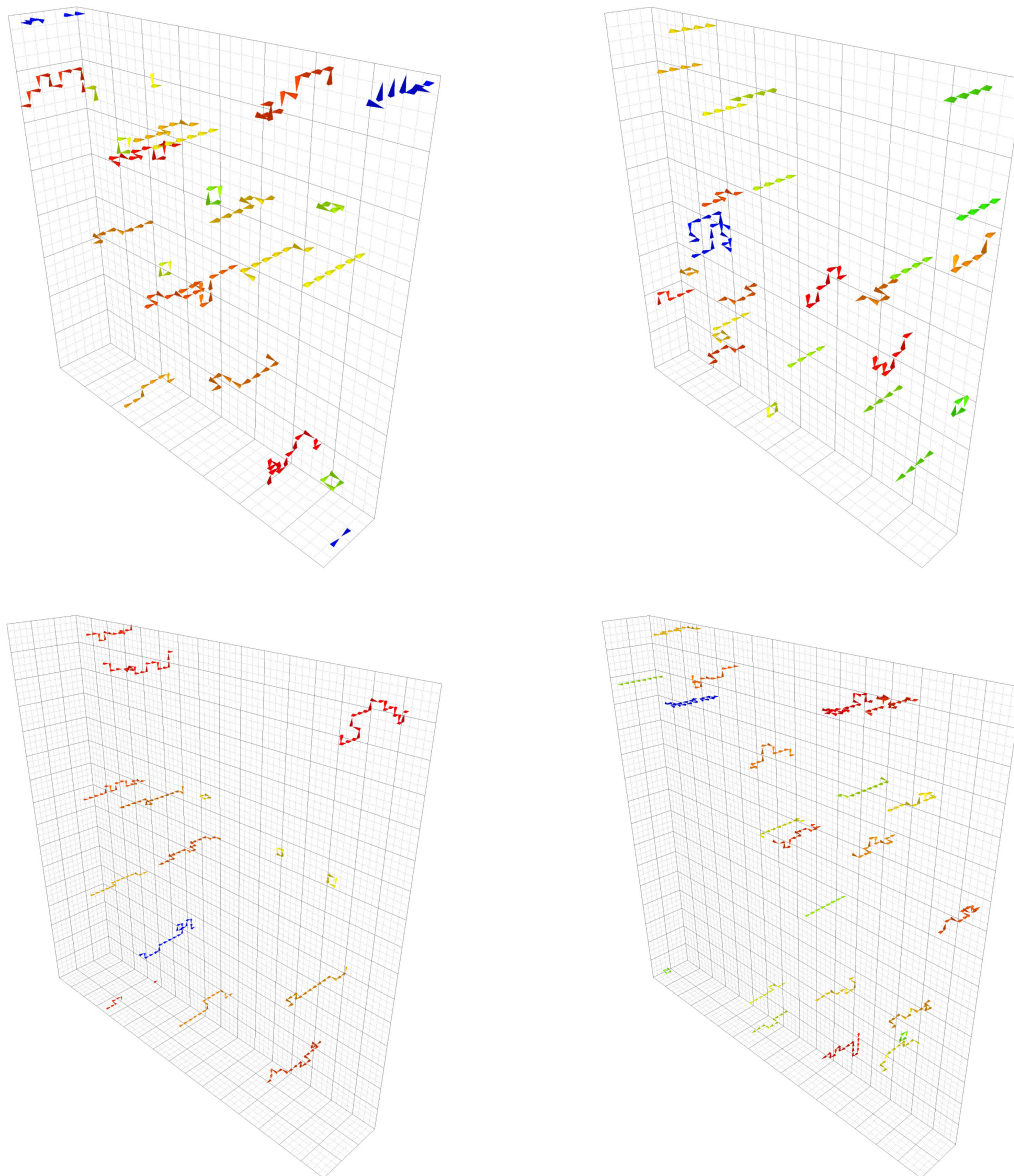
FIG. 9.   Center vortex structure in a single spatial slice for each ensemble used to investigate the vortex sheet alignment with the temporal dimension: $\beta = 5.96$ (top) and $\beta = 6.42$ (bottom), with $T/T_c = 1.218$ (left) and $T/T_c = 1.827$ (right).

though can be converted to a physical quantity ρ_{vortex} by dividing by a^2, which gives proper scaling in the continuum limit [14,15,25].

The evolution of ρ_{vortex} with temperature is presented in Fig. 10, with separate data points for averaging over temporal and spatial slices due to the vastly different structures. As expected, we find a sharp decrease in spatial slices of the lattice as soon as T_c is crossed, coinciding with the absence of a percolating cluster. The area density in the temporal slices also undergoes an initial smaller drop at T_c. Both of these subsequently grow in value above T_c. This is particularly notable in the temporal slices for which ρ_{vortex} proceeds to increase back to below T_c levels. This agrees with the qualitative conclusion reached through the visualizations.

Another curious occurrence is the slight increase in vortex density as T_c is approached from below, as seen with the data points at $T/T_c = 0.913$ in Fig. 10. These sit clearly above the other points below T_c, and is especially pronounced in spatial slices. Greater insight into this behavior can be obtained by decomposing the vortex density in spatial slices to consider the proportion of space-space and space-time plaquettes pierced separately. The space-space density calculated in this manner is equivalent to the vortex density in temporal slices from Fig. 10, which comprise entirely space-space plaquettes. After averaging over all slices of the lattice, every space-space plaquette has been accounted for in both quantities. Accordingly, there must be interesting behavior in the space-time plaquettes that induces the larger density in spatial slices. These
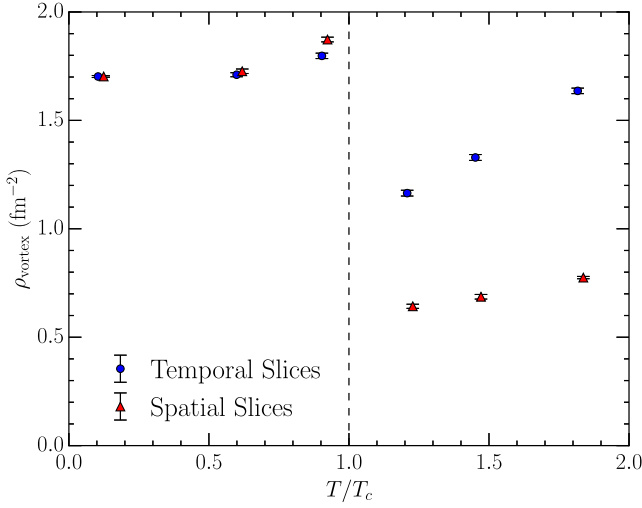
FIG. 10. The vortex area density in temporal and spatial slices of the lattice for each finite-temperature ensemble. The spatial slices experience a significant drop in vortex density at the phase transition, matching the absence of a percolating cluster. There is also an initial drop in the temporal slices, after which it subsequently increases with temperature.
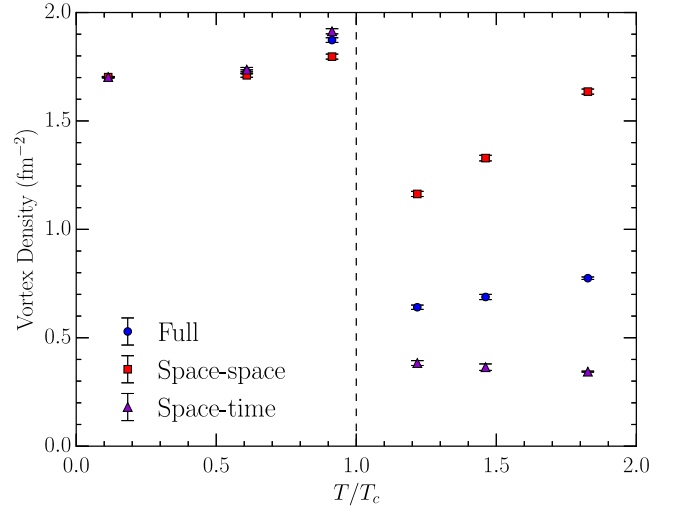
FIG. 11. The physical density of space-space and space-time plaquettes pierced in spatial slices of the lattice. There is a greater density in space-time plaquettes approaching the critical temperature from below. Above T_c, the space-time density is approximately constant whilst the space-space value increases. Combined, this results in the mild increase in the full density.

decomposed densities are shown in Fig. 11, with the "full" spatial density from Fig. 10 overlaid for reference.

It is reassuring that the proportion of space-space plaquettes pierced coincides with the temporal density, as required. Fig. 11 then explicitly reveals a divergence in the density of space-space and space-time plaquettes pierced approaching the phase transition from below, with a larger density of vortices piercing space-time planes. This asymmetry has previously been seen in SU(2) near T_c [19], and accounts for the greater vortex density in spatial slices over temporal slices. In addition, the density in space-time plaquettes remains approximately constant above T_c, which explains why the increase in the "full" density in spatial slices is mild in comparison to that found in temporal slices.

It is now clear why the vortex density in spatial slices exceeds that in temporal slices as the phase transition is approached from below. We understand that deconfinement is associated with an alignment of the vortex sheet with the temporal axis, whereas at low temperatures there is no preferred orientation. Thus, before the deconfinement transition can take place, a rearrangement of the vortex sheet is required, and Fig. 11 reveals this manifests as a preference to pierce space-time plaquettes as it prepares to align with the temporal axis. These will be features to look for in the branching point statistics to ascertain whether they are recurring characteristics across various vortex attributes.

D. Nonpercolating clusters

Next, we investigate the nonpercolating aspects of the center vortex structure. These encompass any cluster seen in Figs. 2–6 that does not spread through the slice volume,

and can be broken down into two distinct categories. First, there are the small structures in temporal slices that contrast the "primary" percolating cluster at all temperatures; these we specifically refer to as "secondary" clusters. The second category concerns spatial slices above T_c where percolation is absent; this grouping therefore covers *all* clusters observed in these slices.

To start, the number of secondary clusters $N_{secondary}$ is presented for the temporal slices in Fig. 12. We note that the notion of "secondary" clusters also applies to spatial slices
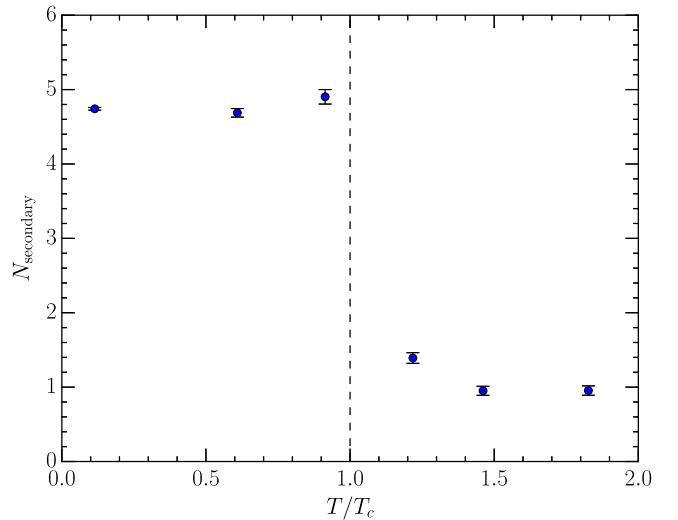
FIG. 12. The temperature-dependence of the average number of secondary vortex clusters $N_{secondary}$ in temporal slices of the lattice. There is a marked drop at the critical temperature, after which there is a continuing decrease.
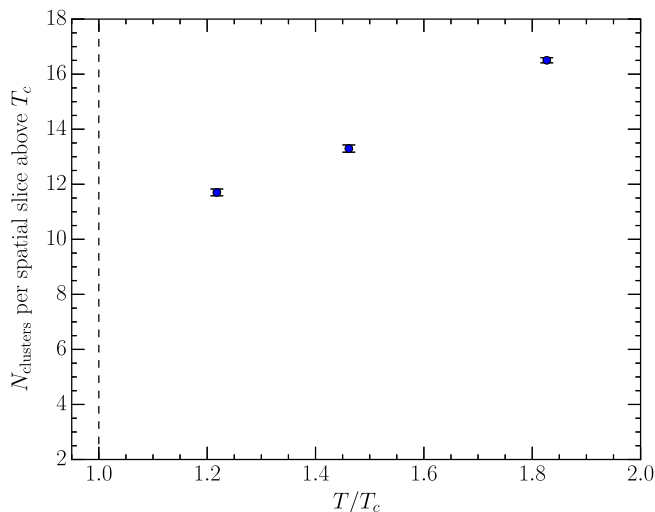
FIG. 13. The average number of vortex clusters per spatial slice above T_c. There is a steady upward trend in the amount of vortex lines as the temperature continues to increase away from T_c. This can be directly attributed to the growing vortex density in temporal slices in this regime.

for $T < T_c$, though our primary focus is directed to temporal slices, which comprise a percolating cluster for all temperatures. This allows an unambiguous exploration on the presence of secondary clusters in the deconfined phase. Figure 12 reveals a pronounced drop in the number of secondary clusters as the critical temperature is crossed. This was suspected from the visualizations. It then continues to decline above T_c to an average of only one secondary cluster per slice at our two highest temperatures. The extent to which $N_{\text{secondary}}$ falls off crossing T_c suggests this is another aspect of vortex geometry that characterizes the deconfinement phase transition in the pure-gauge theory. The decrease above T_c may be partly associated with the increase in vortex density illustrated in Fig. 10. As the volume fills with vortices, there is less space for secondary clusters. That being said, it is currently unclear why high temperatures result in the initial suppression of secondary clusters for $T > T_c$.

Second, we inquire into the number of clusters N_{clusters} per spatial slice above T_c. This is shown in Fig. 13. These are small, mutually disconnected clusters which primarily wind around the temporal dimension, and serve as a basic reflection of the spatial structure seen in time slices. Figure 13 reveals a gradual increase in the number of these clusters with temperature, which was not immediately apparent from the visualizations. This increase is inherently connected to the growing vortex density in temporal slices for $T > T_c$. It follows that when subsequently slicing along a spatial dimension, there are more jets within a given slice. This naturally leads to a greater abundance of vortex lines aligned with the temporal axis in spatial slices.

V. BRANCHING POINT GEOMETRY

Due to the existence of two distinct nontrivial center phases, SU(3) vortices experience vortex branching where an $m = \pm 1$ vortex splits into two $m = \mp 1$ vortices. This is allowed due to the conservation of center charge modulo N. Branching does not occur in SU(2) where there is only a single nontrivial phase. Therefore, branching points offer a unique avenue of investigation into center vortices in SU(3) compared to SU(2).

Since reversing the orientation of a jet indicates the flow of the opposite center charge, branching points can equivalently be interpreted as the monopoles illustrated in Figs. 2–6. Here, three vortices of the same center charge emerge from, or converge to, a single point. A schematic of this equivalence between branching and monopole points is given in Fig. 14. Recalling our visualizations show the flow of $m = +1$ center charge, branching points exclusively appear as monopoles in our visualizations.

A. Branching point density

The first quantity of interest is the branching point density, defined for a given three-dimensional slice as the proportion of elementary cubes that contain a branching point,

$$\hat{\rho}_{\text{branch}} = \frac{\text{Number of branching points in slice}}{V_{\text{slice}}}. \quad (12)$$

As a volume density, the appropriate physical quantity is $\rho_{\text{branch}} = \hat{\rho}_{\text{branch}}/a^3$, which is known to scale correctly as $a \to 0$ [25,38]. Its evolution with temperature is presented in Fig. 15. We find identical patterns to those identified for the vortex area density in both temporal and spatial slices. This includes the peculiar increase near T_c, which is again stronger in spatial slices. That being said, the drop in ρ_{branch} in spatial slices across T_c is even larger than for ρ_{vortex}.
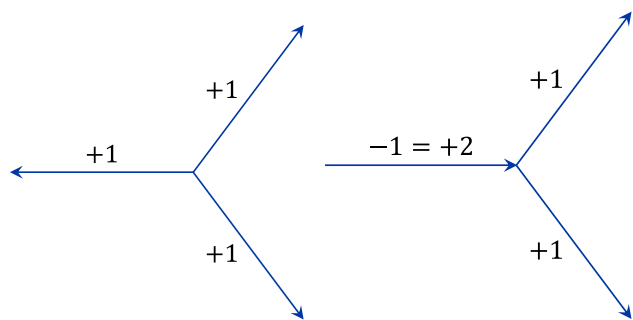

FIG. 14. Schematic of a monopole vertex (left) versus a branching point (right). The monopole vertex follows our convention to illustrate the directed flow of $m = +1$ center charge. Reversal of the left-hand arrow in the diagram shows the flow of charge $m = -1$, as seen on the right. Due to periodicity in the center charge, $m = -1$ is equivalent to $m = +2$. Thus, the right-hand diagram depicts branching of center charge.
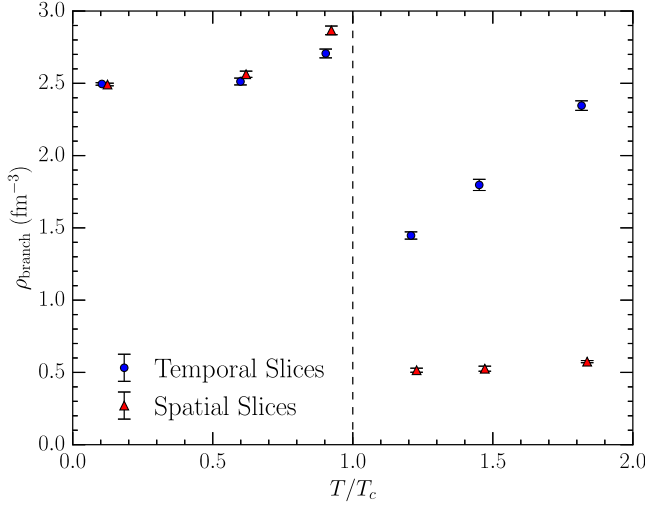
FIG. 15. The density of vortex branching points in temporal and spatial slices of the lattice for each finite-temperature ensemble. The trends in both temporal and spatial slices match those identified for the vortex area density.

This is to be expected—with the vortices principally aligned along the short temporal dimension, there are very few opportunities for the vortex line to branch, resulting in a substantial suppression of ρ_{branch} in spatial slices.

In temporal slices, the increase in ρ_{branch} above T_c is connected to the corresponding behavior of ρ_{vortex}, where an increase in vortex density naturally allows for more branching chances within the same spatial volume. In this scenario a more interesting quantity might be the *linear* branching point density,

$$\hat{\lambda}_{\text{branch}} = \frac{\text{Number of branching points in slice}}{\text{Number of vortices in slice}}, \quad (13)$$

i.e., the proportion of vortices that undergo branching. The corresponding physical quantity is $\lambda_{\text{branch}} = \hat{\lambda}_{\text{branch}}/a$. As defined in Eq. (13), $\hat{\lambda}_{\text{branch}}$ can also be interpreted as an estimate of the average probability per unit length for a vortex to branch. We will see in Sec. V B that this probability is in fact distance dependent.

Following from our definition of λ_{branch}, one finds the below simple relation summarizing how various vortex properties intertwine,

$$\rho_{\text{branch}} = 3\rho_{\text{vortex}}\lambda_{\text{branch}}. \quad (14)$$

This is derived by a straightforward substitution of Eqs. (11)–(13), and noting that the number of vortices in a slice [from the denominator of Eq. (13)] is by definition equal to the number of nontrivial plaquettes [from the numerator of Eq. (11)]. Thus, a constant λ_{branch} would give a clear-cut relationship between the vortex and volume branching point densities. In contrast, if λ_{branch} is also subject to nontrivial evolution with temperature the
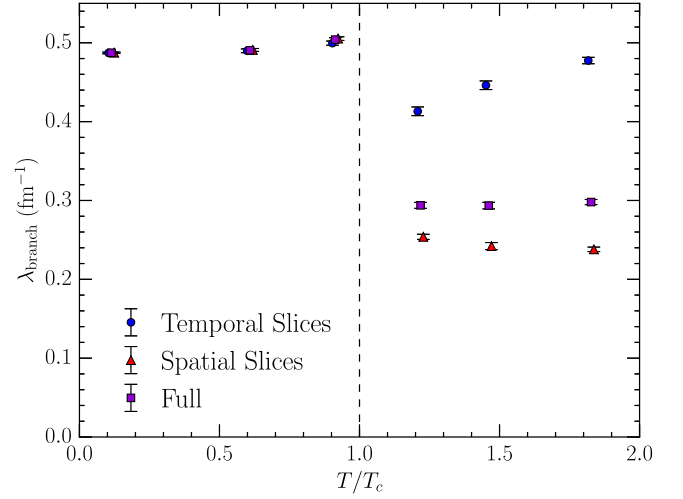

FIG. 16. The linear density of vortex branching points in temporal and spatial slices of the lattice for each finite-temperature ensemble, and a "full" value from averaging over all four slice dimensions. The trends in temporal and spatial slices coincide with those identified for vortex and branching point densities, though are less pronounced. The full dimensionally averaged value is notably constant above T_c.

dependency becomes more complicated. We plot the linear branching point density in temporal and spatial slices as a function of temperature in Fig. 16. This is overlaid by a "full" density $\bar{\lambda}_{\text{branch}}$ obtained by averaging λ_{branch} over all four slice dimensions,

$$\bar{\lambda}_{\text{branch}} = \frac{1}{4}\sum_{\mu}\lambda_{\text{branch}}(\mu), \quad (15)$$

where $\lambda_{\text{branch}}(\mu)$ is the linear branching density for slice dimension μ. This is relevant to the following discussion.

The same general trends are found in λ_{branch} as for ρ_{vortex} and ρ_{branch} but visibly subdued, with a smaller drop at T_c for both temporal and spatial slices. Importantly, the fact λ_{branch} increases in temporal slices above T_c implies the corresponding increase in ρ_{branch} is not solely due to the growing vortex density. It is additionally caused in part by an increase in the inherent fraction of vortices that undergo branching, as per Eq. (14).

We also find that the "full" dimensionally averaged value $\bar{\lambda}_{\text{branch}}$, forgoing the small increase near T_c, remains approximately constant either side of the phase transition (over our temperature range). This value changes when crossing T_c, with the reduced value in the high-temperature phase signifying a corresponding change in the vortex geometry. This can be understood by noting that the shift in vortex geometry to principally align with the temporal axis implies there is generally one less dimension available for a vortex to branch into, explaining why $\bar{\lambda}_{\text{branch}}$ decreases through the phase transition. For a simple heuristic argument, the collapse in vortex geometry from four- to

three-dimensional implies the number of available dimensions for a vortex line within the sheet to branch into decreases from three to two. It follows that at leading order, one might expect the value of $\bar{\lambda}_{\text{branch}}$ to drop by a factor of $2/3$ at T_c. Figure 16 shows reasonable consistency with this proposal, for which taking a ratio between the average values in the two phases yields ≈ 0.60.

The fact $\bar{\lambda}_{\text{branch}}$ subsequently remains constant above T_c, despite the significant differences in spatial and temporal structures, provides a baseline that underlies many of our prior findings at high temperature. The vortex correlation measure (Fig. 8) indicated that the alignment of the vortex sheet with the temporal dimension becomes stronger as the temperature increases above T_c. With $\bar{\lambda}_{\text{branch}}$ constant, this implies that proportionally more of the branching points must occur in temporal slices over spatial slices.

To understand this, recall the alignment manifests in spatial slices as short vortex lines orthogonal to space-space plaquettes, and therefore parallel to the temporal dimension. The occurrence of a branching point would necessitate the piercing of space-time plaquettes, which is suppressed as the alignment becomes stronger. Hence, above T_c the linear branching density decreases in spatial slices, counterbalanced by an increase in temporal slices such that the full density remains constant (as seen in Fig. 16). This evolution naturally effects an increase in the vortex density in temporal slices, where more plaquettes are pierced from the greater proportion of branching vertices. From Eq. (14), there is consequently a compounding effect that results in a substantial increase in the volume density of branching points.

In summary, the constant value of $\bar{\lambda}_{\text{branch}}$ above T_c provides an underlying explanation for why the vortex and branching point densities grow in temporal slices of the lattice in the deconfined phase, in spite of the initial drop they experience across the phase transition. Furthermore, the fact that $\bar{\lambda}_{\text{branch}}$ remains constant whilst the asymmetry between the temporal and spatial extents of the lattice increases with temperature highlights the significance of the vortex geometry in the context of all four dimensions. The geometric nature of the phase transition is understood as a reduction in the dimensionality of vortex percolation from the full four-dimensional lattice to within a three-dimensional submanifold. The primary effect of increasing the temperature in the deconfined phase is an evaporation of branching points from spatial slices as the vortex geometry aligns with the temporal axis, with a commensurate condensation of branching points on temporal slices in exchange such that the average linear branching probability remains constant.

B. Branching point separations

In Sec. V A the bulk properties of branching points were investigated, which we presently extend to a detailed analysis of the intrinsic distribution of branching points throughout the vortex structure. A model for vortex branching proposes that a vortex line has a fixed probability of branching as it propagates through space-time [38]. It follows that the path lengths between consecutive branching points on the lattice would be described by the geometric distribution,

$$\Pr(k) = p(1-p)^{k-1}, \tag{16}$$

for branching probability p and number of trials k.

This has previously been tested at zero temperature in Ref. [48] by devising an algorithm to determine the separations between branching points and producing a histogram of the results. The conjecture was supported for separations > 3 where it was found the distribution is approximately exponential. This is spoiled at short distances due to a tendency for branching points to cluster near each other. It is for this reason $\hat{\lambda}_{\text{branch}}$ defined in Eq. (13) fails to provide a reliable estimate of the branching probability.

To determine the probability p, a linear function

$$f(k) = \alpha - \beta k \tag{17}$$

is fit to the log of the distribution for separations $k > 3$, which by comparing to the logarithm of Eq. (16) allows one to extract the corresponding long-range branching probability from the slope parameter β as

$$p = 1 - e^{-\beta}. \tag{18}$$

We utilize the algorithm of Ref. [48] to explore how, if at all, this geometry of branching points and the associated branching probability depends on temperature.

These distributions are shown independently for temporal slices in Fig. 17 and spatial slices in Fig. 18. In the confined phase, the distributions for both temporal and spatial slices are all extremely similar, each featuring the aforementioned clustering at branching point separations ≤ 3 before a steep falloff in probability leads into a smooth long-range exponential trend.

Above T_c, the branching point geometry for temporal and spatial slices diverges, with opposing trends to be found. In spatial slices, the probability of small separations only becomes more pronounced, as is apparent by the height of the respective histogram bins in Fig. 18. However, this is presumably an artificial change that arises from the absence of percolation in the deconfined phase, and the alignment of the vortex sheet with the temporal dimension. As seen in the visualizations (Figs. 4–6), the spatial slices therefore consist of many short vortex lines parallel to the temporal axis.

Consequently, large branching point separations are suppressed, with path lengths $\gtrsim N_t$ becoming increasingly rare. Owing to the very low statistics at large separations,
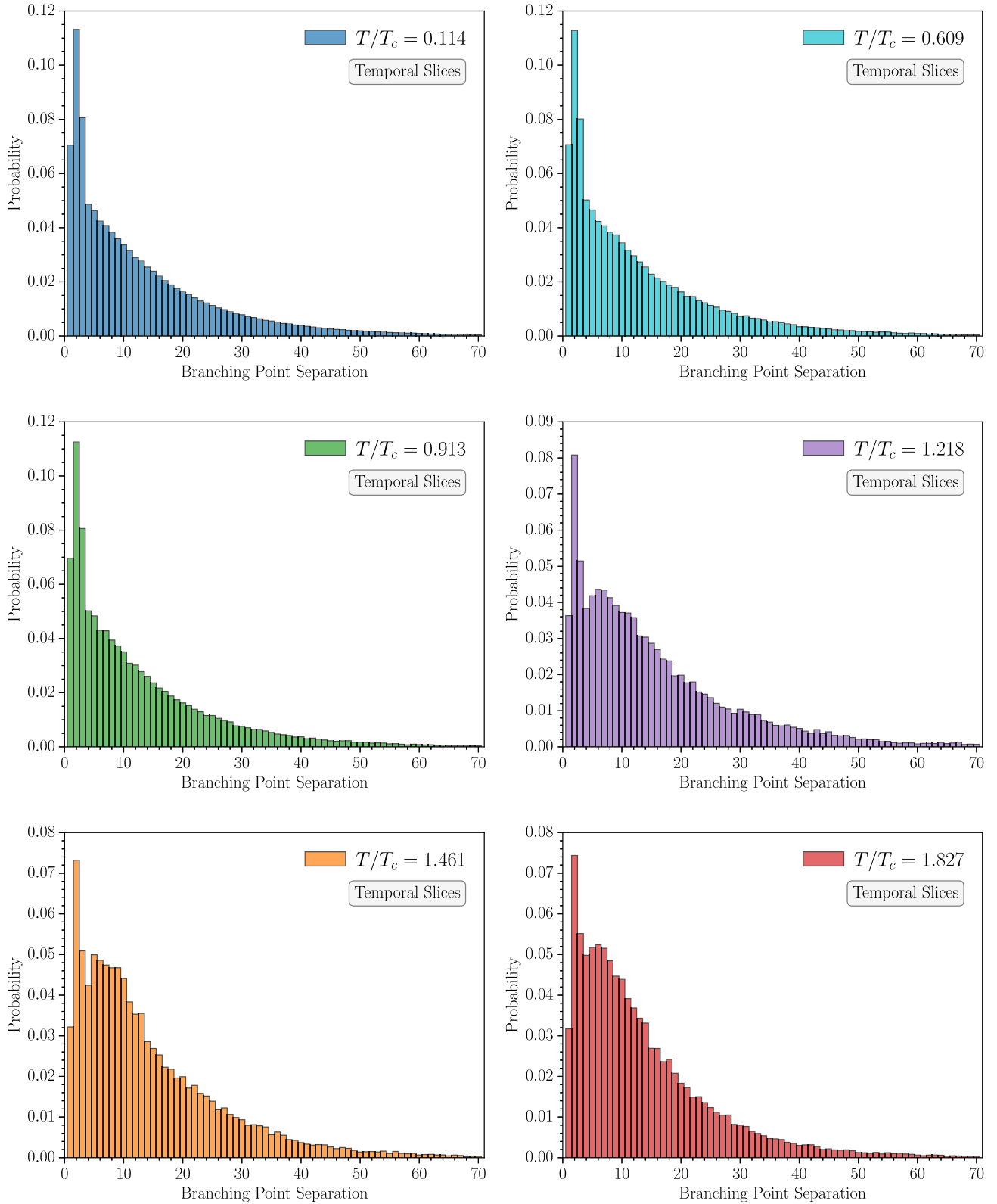
FIG. 17. The distribution of branching point separations, k, in temporal slices of the lattice for each finite-temperature ensemble. The histograms are normalized to unit probability. Below T_c the distributions are similar, exhibiting a clear clustering at separations $k \leq 3$ with a smooth exponential falloff. Above T_c the clustering is visibly softened, and there is also a reduction in probability at separations $k = 4$ and 5.
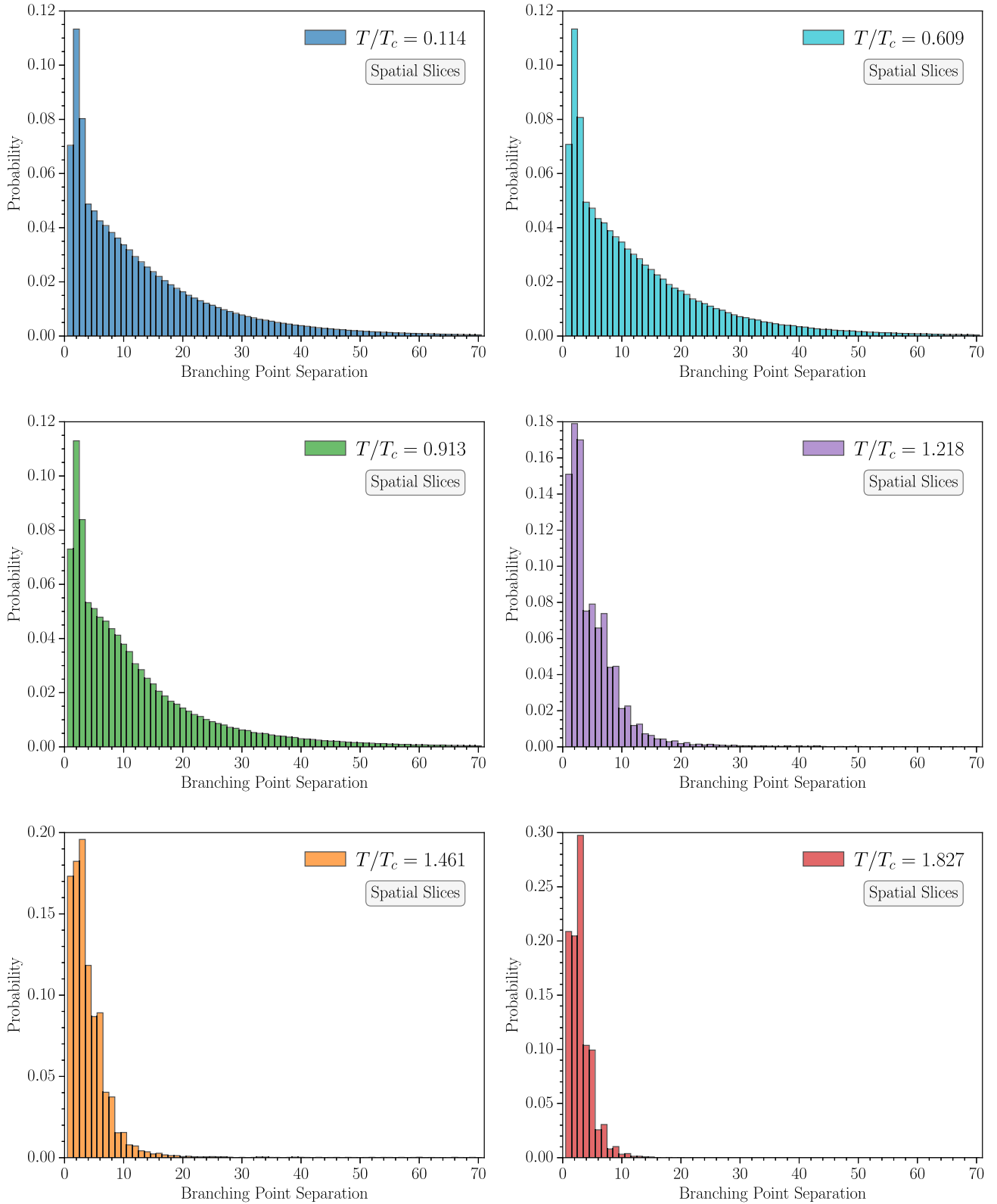
FIG. 18. The distribution of branching point separations, k, in spatial slices of the lattice for each finite-temperature ensemble. The histograms are normalized to unit probability. Below T_c, the distributions coincide with that seen in the temporal slices. Above T_c, the probability of short separations is increased owing to the alignment of vortices along the temporal dimension, meaning separations $k > N_t$ become increasingly rare.

and the sporadic distribution at short distances, performing the aforementioned fits to our spatial slices data above T_c is infeasible. As a result, we refrain from estimating the branching probability in spatial slices. We propose that a possible method to overcome this limitation is to introduce anisotropy into the lattice along the temporal dimension. At high temperatures, this would allow for more branching chances in spatial slices and permit greater distances (in lattice units) between successive branching points. The fits might then successfully be performed over an adequate range of separations.

In contrast, the clustering in temporal slices is diminished in the deconfined phase and continues to subside as the temperature grows. Moreover, this decline in probability at small distances extends to separations $k = 4$ and 5, where above T_c we have $\Pr(4) < \Pr(5) < \Pr(6)$. The familiar exponential decay then takes effect for $k \geq 6$, which is evident from Fig. 17. This time the lack of a constant branching probability at short distances is no longer due to a *clustering*, but instead due to a *dilution* of branching points at short- to mid-range scales. Given the temporal center vortex structure comprises a percolating cluster in both phases, we can be confident this is a genuine shift in the intrinsic arrangement of branching points, rather than arising from an external change in vortex geometry. For instance, the branching point densities in temporal slices are extremely similar at our highest temperature $T/T_c = 1.827$ compared to below T_c (Figs. 15 and 16), though the inherent distribution of these branching points is plainly very different.

In Ref. [48], it was questioned whether the clustering radius at low temperatures is a physical effect, or a discretization artefact of a nonzero lattice spacing. Based on the above discussion, we propose it is a physical effect that vanishes at high temperatures (in temporal slices).

Having carefully analyzed these distributions, we now proceed to determine the branching probability as a function of temperature. To avoid uncertainty asymmetry induced by taking the log of the data, we utilize a slightly different method to Ref. [48] and instead perform a direct exponential fit,

$$f(k) = \zeta e^{-\lambda k}, \tag{19}$$

to the *raw* counts, where ζ is a normalization parameter. The connection between the exponential and geometric distributions (see Appendix) allows us to estimate the branching probability for our discrete data as

$$p_{\text{branch}} = 1 - e^{-\lambda}, \tag{20}$$

cf. Eq. (18). To be precise in our methods, we initially perform the linear fit to the logarithm of the counts. The output of this fit is then used to provide accurate initial guesses to the nonlinear exponential fit, $\zeta = e^{\alpha}$ and $\lambda = \beta$.

We find the exponential fit converges to a marginally (but visibly) different optimal solution. This is taken as our best estimate of the model.

To account for the $T > T_c$ behavior discussed above, we perform the fit at all temperatures only for separations $k > 5$ and exclusively in temporal slices. This procedure is carried out on 100 bootstrap ensembles, allowing an uncertainty to be placed on the final probability. For each bootstrap sample, Poisson square-root errors are placed on the histogram bin counts for incorporation into the least-squares fit. The fits for each ensemble are shown on a logarithmic scale in Fig. 19, and the resulting evolution of the branching probability is presented in Fig. 20.

The fits of Fig. 19 are observed to describe the data well. The suppression of short-distance clustering at high temperatures is abundantly clear. The lower statistics at large distances is especially pronounced for the higher-temperature ensembles, which have less statistics by default. For completeness, we reperform the fits exclusively including up to a maximum separation of $k_{\text{max}} = 50$, which is additionally shown in Fig. 20. Incorporating this cutoff is seen to have a visible but ultimately insignificant effect, justifying the original fits.

It is expected that the branching probability scales with the lattice spacing [38]. This can be intuitively understood by the fact vortex and branching point densities are known to exhibit scale invariance as $a \to 0$. Thus if one were to decrease a, the position of vortices would be resolved to greater precision, but the physical distance between branching points would be unchanged. In other words, the probability of branching in a given elementary cube would decrease proportionally to the lattice spacing. For this reason, Fig. 20 shows a physical "probability per unit length" by dividing the value obtained through the fits by our lattice spacing of $a = 0.1$ fm.

The branching probability displays the same general trends as the previous vortex quantities investigated, including the mild increase approaching T_c from below, the drop through the phase transition and the steady climb in value as the temperature rises above T_c. That being said, the cut in probability at the critical temperature is much less pronounced here, and its value is then amplified to notably exceed below T_c levels at our highest temperature.

It is prescient to compare this behavior to the linear branching point density (Fig. 16), where if a constant branching probability held over all separations these measures would be expected to coincide. Instead, the probability obtained through the fits is found to consistently sit above the linear density at all temperatures, consistent with the previous finding at zero temperature [48].

This is a consequence of incorporating the short-distance physics into the naive linear branching density, incompatible with the constant probability picture at large separations. Of utmost interest is the high-temperature behavior,
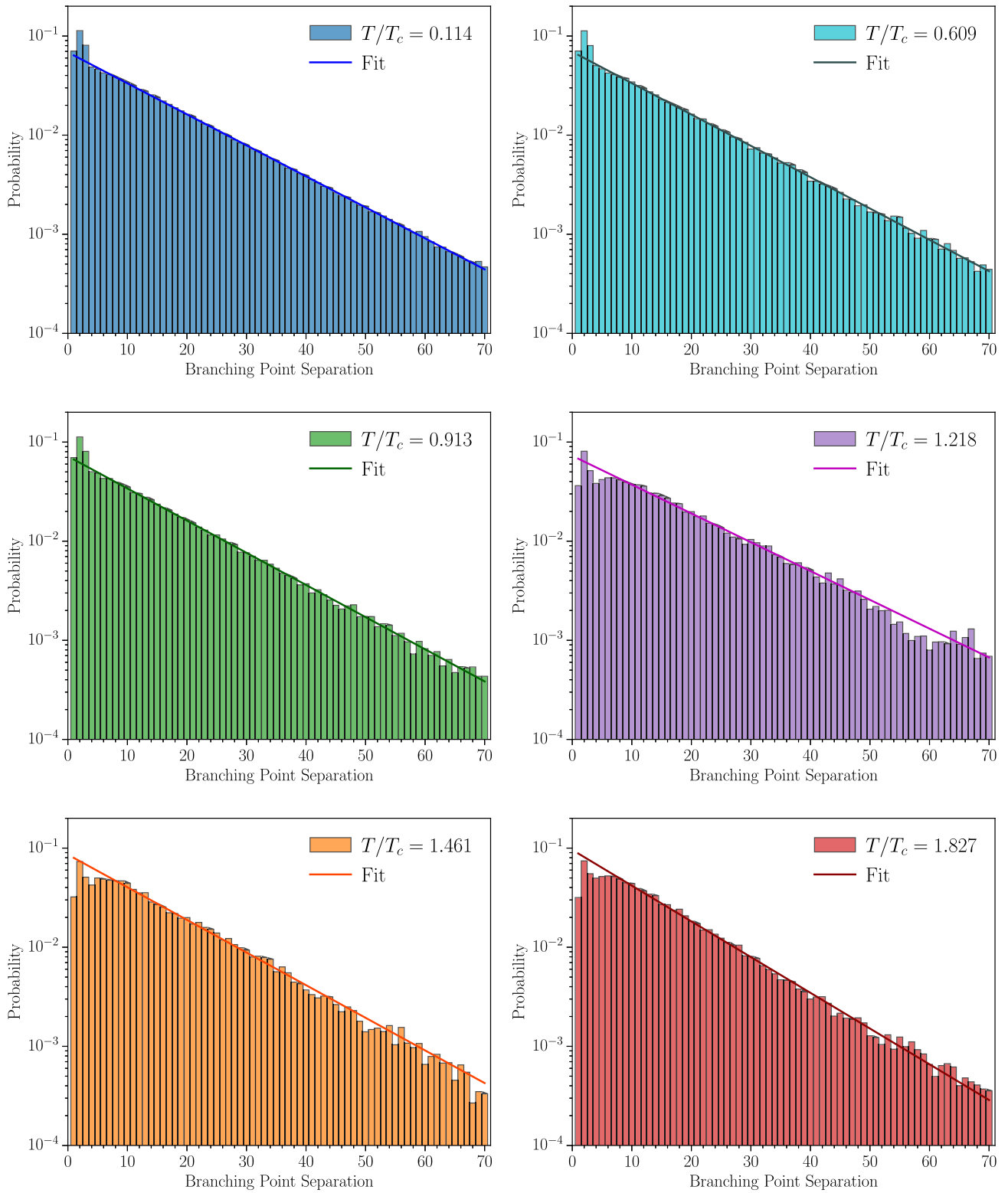
FIG. 19. The distribution of branching point separations, k, on a logarithmic scale in temporal slices of the lattice for each finite-temperature ensemble. The exponential fits are overlaid on the histograms, and evidently match the data well barring at very high separations where there is insufficient statistics. The reduction in density at short distances above T_c is visually clear in these plots, with most of the probabilities for separations $k \leq 5$ sitting below the fits.
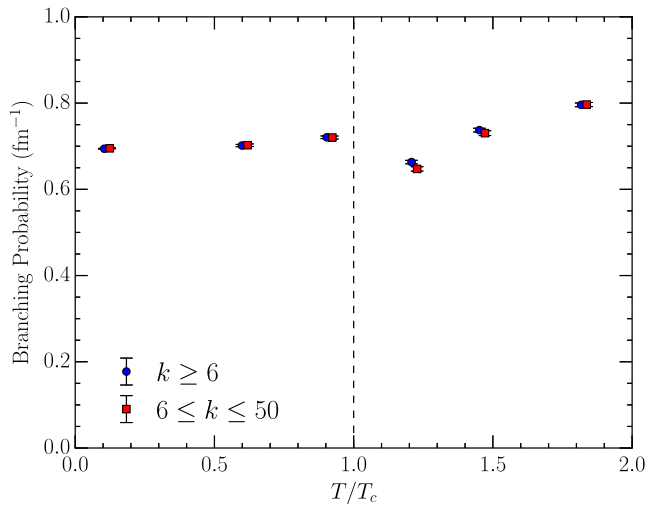
FIG. 20. The long-range ($k \geq 6$) branching probability of a vortex line as a function of temperature, estimated by performing an exponential fit to the distribution of branching point separations. There is a mild drop in the branching probability across the phase transition, which subsequently increases to a value markedly exceeding the below T_c values. Including a cutoff $k \leq 50$ to account for low statistics at large distances is seen to have minimal effect on the results.

where although the linear density never exceeds the below T_c values over our temperature range, the branching probability does by a considerable margin. That is to say, the long-distance probability of a vortex undergoing branching is greater at very high temperatures compared to low temperatures. This conclusion was obscured in the linear density, which highlights the importance of separating out the short-distance behavior in providing a comprehensive assessment of branching point geometry.

VI. CONCLUSION

In this paper we have explored the evolution of pure-gauge SU(3) center vortex structures with temperature. Initially, a qualitative discussion was presented by visualizing the vortex structure in temporal and spatial slices of the lattice. This established a shift in the center vortex sheet to principally align with the short temporal dimension in the deconfined phase. As a consequence, the vortex cluster is observed to be primarily frozen between temporal slices of the lattice. By aligning with the temporal axis, the vortex sheet rarely cuts through space-time plaquettes above T_c. This is reflected in spatial slices, where the majority of vortices pierce space-space plaquettes and are therefore oriented in the temporal dimension. In other words, this manifests as many short vortex lines chiefly parallel to the temporal axis.

An array of vortex statistics was calculated to investigate additional intrinsic changes to the vortex structure. These statistics include the vortex density, and volume and linear branching point densities. All of these measures exhibit the same overarching trend. Crossing the phase transition, each quantity experiences a cut in value in both temporal and spatial slices, though this was less pronounced in temporal slices. These values in the temporal slices subsequently increase as the temperature continues to rise above T_c, returning to below T_c levels by the highest temperature considered $T/T_c \approx 1.827$.

Decomposing the density in spatial slices to consider space-space and space-time plaquettes independently revealed a slight preference of the vortex sheet to pierce space-time plaquettes as the temperature nears T_c. We propose this is a necessity as the vortex sheet prepares to align with the temporal dimension. Other peculiar findings, such as an increase in each of the aforementioned statistics whilst approaching the phase transition from below, and a major suppression of secondary clusters above T_c, warrant further investigation into their cause. This could be achieved by focusing on a narrower range of temperatures near T_c, or utilizing finer lattices to study the scaling behavior of these trends.

Calculating a linear branching density averaged over spatial and temporal slices revealed constant (but distinct) values on both sides of the phase transition. This is in spite of the strong asymmetry between the space and time slices above T_c. This embodies a degree of "locking" in the vortex structure, in which continued changes in spatial slices of the lattice must be counteracted by an opposite trend in temporal slices. This opens the possibility of an underlying symmetry connected with the vortex topology which results in the average linear branching probability becoming an effective constant. In future work, it will be interesting to investigate this quantity over an extended temperature range, both nearer to and farther from T_c, to ascertain the extent to which this locking persists in the deconfined phase.

Finally, we explored changes to the inherent distribution of branching points throughout the vortex clusters with temperature. Here, we find a tendency of branching points to cluster at short separations at low temperatures is lost as we move through the phase transition. At large separations, their distribution can nonetheless be described by a constant branching probability. This long-distance probability is decidedly greater at very high temperatures compared to low temperatures. Thus, branching is enhanced at very high temperatures.

By analyzing other topological aspects of the gauge fields, it was proposed in Ref. [50] that full QCD experiences a second phase transition at a higher temperature $T \approx 2T_c$. This was based on the behavior of the Polyakov loop in different nontrivial representations of SU(3) and the topological index of gauge field configurations. Although our results on center vortex structure do not evince any evidence for such a second transition, this could be due to the limited temperature range considered or the nature of pure gauge theory compared to full QCD. There is the possibility for further investigation in this regard by

utilizing the finer resolution provided by an anisotropic lattice to consider a greater range of temperatures.

Future work will extend this analysis to include the effect of dynamical fermions on center vortices at finite temperature. This has previously been conducted at zero temperature [48], where many quantities of interest, such as the number of secondary clusters, vortex, and branching point densities, and the degree of clustering at short separations are observed to significantly increase. Hence it will be interesting to see the extent to which the findings on vortex geometry through the phase transition presented herein are impacted (or otherwise) by the inclusion of dynamical fermions.

APPENDIX: EXPONENTIAL AND GEOMETRIC DISTRIBUTIONS

In this appendix we derive the connection between the exponential and geometric distributions used to extract an estimate of the branching probability from our exponential fits, Eq. (19). If a continuous random variable Y follows an exponential distribution, $Y \sim \text{Exp}(\lambda)$, it has the (normalized) probability density

$$f(x; \lambda) = \lambda e^{-\lambda x}. \tag{A1}$$

The discrete random variable $X = \lfloor Y \rfloor + 1$, supported on the set $\{1, 2, 3, \dots\}$, then follows a geometric distribution,

$$\begin{aligned}
\Pr(X = k) &= \Pr(k - 1 \leq Y < k), \\
&= \int_{k-1}^{k} dx\, \lambda e^{-\lambda x}, \\
&= e^{-\lambda(k-1)} - e^{-\lambda k}, \\
&= (1 - e^{-\lambda}) e^{-\lambda(k-1)}, \\
&= (1 - e^{-\lambda})[1 - (1 - e^{-\lambda})]^{k-1}. \tag{A2}
\end{aligned}$$

This coincides with the formula for a geometric distribution, Eq. (16), with probability of success

$$p = 1 - e^{-\lambda}. \tag{A3}$$

This verifies Eq. (20) for the branching probability, where the random variable X is identified with the branching point separations. Note that in our fits, we necessarily included an unconstrained normalization parameter ζ to accommodate the nonexponential behavior at short separations. However, this has no effect on the above probability, but rather just carries through to an equivalent normalization factor in the geometric distribution.

[1] G. 't Hooft, On the phase transition towards permanent quark confinement, Nucl. Phys. **B138**, 1 (1978).

[2] G. 't Hooft, A property of electric and magnetic flux in non-Abelian gauge theories, Nucl. Phys. **B153**, 141 (1979).

[3] H. B. Nielsen and P. Olesen, A quantum liquid model for the QCD vacuum: Gauge and rotational invariance of domained and quantized homogeneous color fields, Nucl. Phys. **B160**, 380 (1979).

[4] J. Greensite, The confinement problem in lattice gauge theory, Prog. Part. Nucl. Phys. **51**, 1 (2003).

[5] P. de Forcrand and M. D'Elia, Relevance of center vortices to QCD, Phys. Rev. Lett. **82**, 4582 (1999).

[6] J. Gattnar, C. Gattringer, K. Langfeld, H. Reinhardt, A. Schäfer, S. Solbrig, and T. Tok, Center vortices and Dirac eigenmodes in SU(2) lattice gauge theory, Nucl. Phys. **B716**, 105 (2005).

[7] P. O. Bowman, K. Langfeld, D. B. Leinweber, A. O' Cais, A. Sternbeck, L. von Smekal, and A. G. Williams, Center vortices and the quark propagator in SU(2) gauge theory, Phys. Rev. D **78**, 054509 (2008).

[8] P. O. Bowman, K. Langfeld, D. B. Leinweber, A. Sternbeck, L. von Smekal, and A. G. Williams, Role of center vortices in chiral symmetry breaking in SU(3) gauge theory, Phys. Rev. D **84**, 034501 (2011).

[9] E.-A. O'Malley, W. Kamleh, D. Leinweber, and P. Moran, $SU(3)$ centre vortices underpin confinement and dynamical chiral symmetry breaking, Phys. Rev. D **86**, 054503 (2012).

[10] A. Trewartha, W. Kamleh, and D. Leinweber, Evidence that centre vortices underpin dynamical chiral symmetry breaking in SU(3) gauge theory, Phys. Lett. B **747,** 373 (2015).

[11] A. Trewartha, W. Kamleh, and D. Leinweber, Centre vortex removal restores chiral symmetry, J. Phys. G **44,** 125002 (2017).

[12] L. Del Debbio, M. Faber, J. Greensite, and Š. Olejník, Center dominance and Z_2 vortices in SU(2) lattice gauge theory, Phys. Rev. D **55,** 2298 (1997).

[13] L. Del Debbio, M. Faber, J. Greensite, and Š. Olejník, Center vortices and the asymptotic string tension, Nucl. Phys. B, Proc. Suppl. **63,** 552 (1998).

[14] K. Langfeld, H. Reinhardt, and O. Tennert, Confinement and scaling of the vortex vacuum of SU(2) lattice gauge theory, Phys. Lett. B **419,** 317 (1998).

[15] L. Del Debbio, M. Faber, J. Giedt, J. Greensite, and Š. Olejník, Detection of center vortices in the lattice Yang-Mills vacuum, Phys. Rev. D **58,** 094501 (1998).

[16] M. Faber, J. Greensite, and Š. Olejník, Casimir scaling from center vortices: Towards an understanding of the adjoint string tension, Phys. Rev. D **57,** 2603 (1998).

[17] M. Faber, J. Greensite, and Š. Olejník, Evidence for a center vortex origin of the adjoint string tension, Acta Phys. Slovaca **49,** 177 (1999), http://www.physics.sk/aps/pub.php?y=1999&pub=aps-99-02.

[18] K. Langfeld, O. Tennert, M. Engelhardt, and H. Reinhardt, Center vortices of Yang-Mills theory at finite temperatures, Phys. Lett. B **452,** 301 (1999).

[19] R. Bertle, M. Faber, J. Greensite, and Š. Olejník, The structure of projected center vortices in lattice gauge theory, J. High Energy Phys. 03 (1999) 019.

[20] M. Engelhardt, K. Langfeld, H. Reinhardt, and O. Tennert, Deconfinement in SU(2) Yang-Mills theory as a center vortex percolation transition, Phys. Rev. D **61,** 054504 (2000).

[21] M. Engelhardt and H. Reinhardt, Center vortex model for the infrared sector of Yang-Mills theory—confinement and deconfinement, Nucl. Phys. **B585,** 591 (2000).

[22] M. Faber, J. Greensite, and Š. Olejník, First evidence for center dominance in SU(3) lattice gauge theory, Phys. Lett. B **474,** 177 (2000).

[23] P. de Forcrand and M. Pepe, Center vortices and monopoles without lattice Gribov copies, Nucl. Phys. **B598,** 557 (2001).

[24] K. Langfeld, H. Reinhardt, and J. Gattnar, Gluon propagator and quark confinement, Nucl. Phys. **B621,** 131 (2002).

[25] K. Langfeld, Vortex structures in pure SU(3) lattice gauge theory, Phys. Rev. D **69,** 014503 (2004).

[26] M. Engelhardt, M. Quandt, and H. Reinhardt, Center vortex model for the infrared sector of $SU(3)$ Yang-Mills theory—confinement and deconfinement, Nucl. Phys. **B685,** 227 (2004).

[27] J. C. Biddle, W. Kamleh, and D. B. Leinweber, Static quark potential from center vortices in the presence of dynamical fermions, Phys. Rev. D **106,** 054505 (2022).

[28] J. C. Biddle, W. Kamleh, and D. B. Leinweber, Impact of dynamical fermions on the center vortex gluon propagator, Phys. Rev. D **106,** 014506 (2022).

[29] M. Engelhardt, K. Langfeld, H. Reinhardt, and O. Tennert, Interaction of confining vortices in SU(2) lattice gauge theory, Phys. Lett. B **431,** 141 (1998).

[30] J. Greensite, Confinement from center vortices: A review of old and new results, EPJ Web Conf. **137,** 01009 (2017).

[31] K. G. Wilson, Confinement of quarks, Phys. Rev. D **10,** 2445 (1974).

[32] J. B. Kogut, An introduction to lattice gauge theory and spin systems, Rev. Mod. Phys. **51,** 659 (1979).

[33] H. G. Dosch and Y. A. Simonov, The area law of the Wilson loop and vacuum field correlators, Phys. Lett. B **205,** 339 (1988).

[34] G. S. Bali, H. Neff, T. Düssel, T. Lippert, and K. Schilling (SESAM Collaboration), Observation of string breaking in QCD, Phys. Rev. D **71,** 114513 (2005).

[35] C. A. Aubin and M. C. Ogilvie, Lattice gauge fixing and the violation of spectral positivity, Phys. Lett. B **570,** 59 (2003).

[36] P. O. Bowman, U. M. Heller, D. B. Leinweber, M. B. Parappilly, A. Sternbeck, L. von Smekal, A. G. Williams, and J. Zhang, Scaling behavior and positivity violation of the gluon propagator in full QCD, Phys. Rev. D **76,** 094505 (2007).

[37] J. C. Biddle, W. Kamleh, and D. B. Leinweber, Visualization of center vortex structure, Phys. Rev. D **102,** 034504 (2020).

[38] F. Spengler, M. Quandt, and H. Reinhardt, Branching of center vortices in SU(3) lattice gauge theory, Phys. Rev. D **98,** 094508 (2018).

[39] See the Supplemental Material at http://link.aps.org/supplemental/10.1103/PhysRevD.110.034516 for interactive animations of the center vortex structure embedded in the text, expanding on the static images presented in the main text. Instructions on interacting with the animations is provided therein.

[40] A. Montero, Study of SU(3) vortex-like configurations with a new maximal center gauge fixing method, Phys. Lett. B **467,** 106 (1999).

[41] M. Faber, J. Greensite, Š. Olejník, and D. Yamada, The vortex-finding property of maximal center (and other) gauges, J. High Energy Phys. 12 (1999) 012.

[42] M. Ghanbarpour and L. von Smekal, Quarks and triality in a finite volume, Phys. Rev. D **106,** 054513 (2022).

[43] S. Duane, A. D. Kennedy, B. J. Pendleton, and D. Roweth, Hybrid Monte Carlo, Phys. Lett. B **195,** 216 (1987).

[44] W. Kamleh, D. B. Leinweber, and A. G. Williams, Hybrid Monte Carlo algorithm with fat link fermion actions, Phys. Rev. D **70,** 014502 (2004).

[45] Y. Iwasaki, Renormalization group analysis of lattice theories and improved lattice action. II. Four-dimensional non-Abelian SU(N) gauge model, arXiv:1111.7054.

[46] Y. Iwasaki, K. Kanaya, T. Kaneko, and T. Yoshié, Scaling in SU(3) pure gauge theory with a renormalization-group-improved action, Phys. Rev. D **56,** 151 (1997).

[47] F. Karsch, Lattice QCD at finite temperature and density, Nucl. Phys. B, Proc. Suppl. **83,** 14 (2000).

[48] J. C. Biddle, W. Kamleh, and D. B. Leinweber, Center vortex structure in the presence of dynamical fermions, Phys. Rev. D **107,** 094507 (2023).

[49] S. Necco and R. Sommer, The $N_f = 0$ heavy quark potential from short to intermediate distances, Nucl. Phys. **B622,** 328 (2002).

[50] M. Hanada, H. Ohata, H. Shimada, and H. Watanabe, A new perspective on thermal transition in QCD, Prog. Theor. Exp. Phys. **2024,** 041B02 (2024).